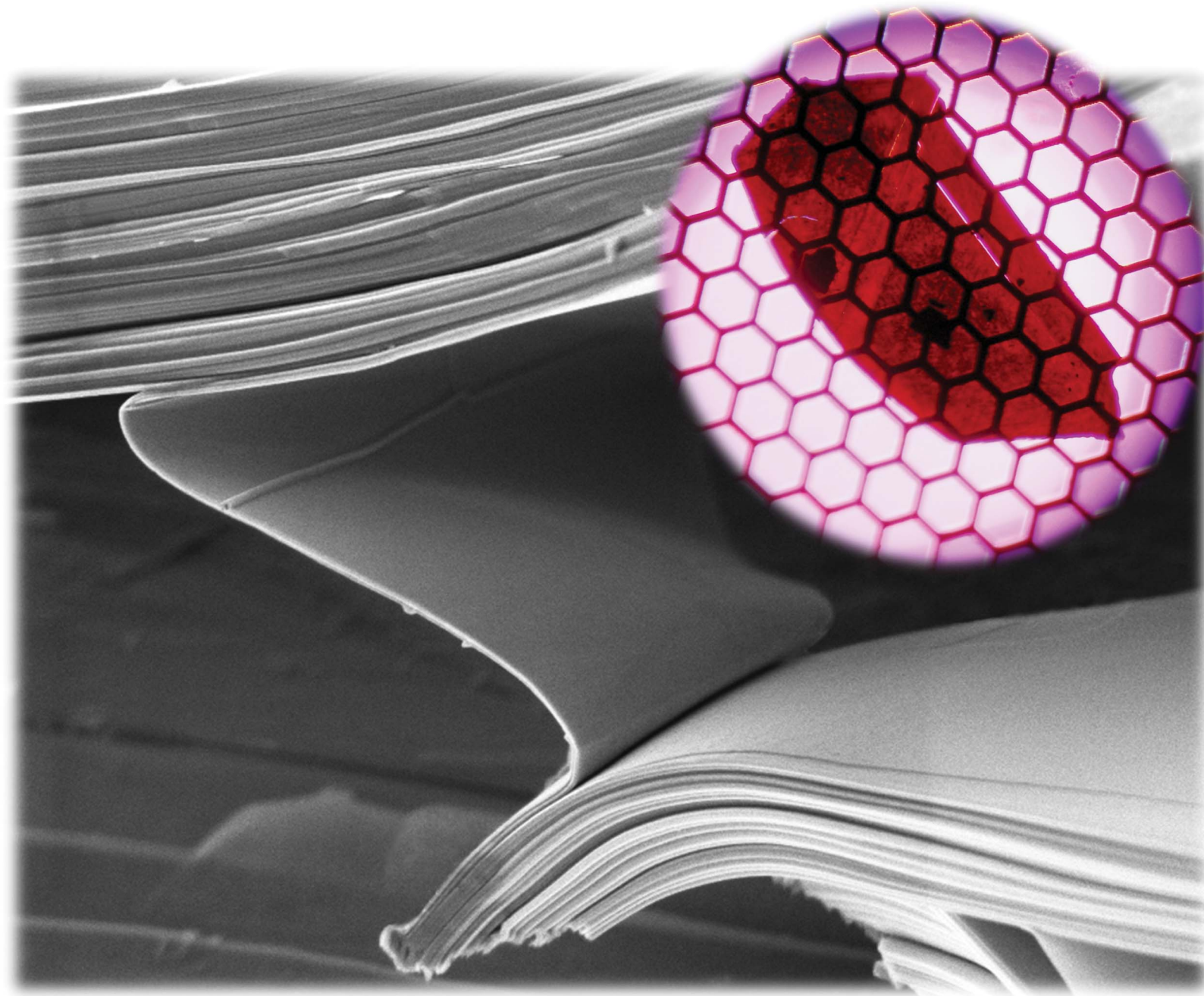


Journal of Materials Chemistry

www.rsc.org/materials

Volume 22 | Number 13 | 7 April 2012 | Pages 5867–6492



ISSN 0959-9428

RSC Publishing

PAPER

Richard D. Robinson *et al.*

Scalable nanomanufacturing of millimetre-length 2D Na_xCoO_2 nanosheets



0959-9428 (2012) 22:13;1-J

Scalable nanomanufacturing of millimetre-length 2D Na_xCoO_2 nanosheets†

Mahmut Aksit, David P. Toledo and Richard D. Robinson*

Received 30th October 2011, Accepted 20th December 2011

DOI: 10.1039/c2jm15550h

A novel, scalable nanomanufacturing technique is reported for batch fabrication of nanoscale-thick $\text{Na}_{0.7}\text{CoO}_2$ nanosheets. The nanomanufacturing technique is a high-yield, bottom-up process that is capable of producing tens of thousands of nanosheets stacked into a macro-scale pellet. The nanosheets are uniform in length and shape with very high crystal anisotropy. The nanosheet thicknesses can be 10–100 nm while their lengths can measure up to 1.8 mm long. The typical dimension ratios are highly anisotropic, at 10^{-5} :1 : 1 (thickness:length:width). X-ray synchrotron studies indicate that the 2D crystals are stacked in a turbostratic arrangement with rotational misalignment with respect to the stacking axis. The stacked nanosheets are readily delaminated into very large ($350\ \mu\text{m} \times 150\ \mu\text{m} \times 100\ \text{nm}$) free-standing 2D crystals. The novel nanomanufacturing technique is based on sol–gel and electric-field induced kinetic-demixing followed by a brief high temperature treatment, thus providing an efficient means of large scale crystal growth requiring only a simple furnace and power supply. Evidence shows that the demixing process increases the concentration of Na ions and that demixing is necessary to produce the millimetre-length nanosheets. Electric field induced kinetic-demixing is successfully performed at low temperatures ($<300\ ^\circ\text{C}$), which is more than three times lower than past kinetic-demixing temperatures.

Introduction

Two-dimensional (2D) oxide crystals present exciting opportunities for new scientific and technological breakthroughs with their novel electronic, ferromagnetic, magneto-optical, electrochemical, catalytic, and photoresponsive properties.^{1–5} Although graphene has been well studied, the synthesis of free-standing 2D nanosheet materials still constitutes a largely unexplored area of nanoscience, especially with inorganic compounds such as transition metal oxides.^{1–3,6}

2D metal oxide nanostructures have great potential for practical applications. Nanosheets of $\text{RuO}_{2.1}$ indicated high performance as electro-chemical supercapacitors.⁷ Reassembled $\text{Ti}_{0.91}\text{O}_2$ and MnO_2 nanosheets showed electrochemical capacities comparable to Li-Ion batteries.^{5,8,9} N-type photo-semiconducting nanosheets of $\text{Sr}_2\text{Nb}_3\text{O}_{10}$ were recently shown to have diode type characteristics in nanosheet p-n junctions.¹⁰ $\text{Ti}_{0.91}\text{O}_2$ and $\text{Ti}_{0.87}\text{O}_2$ nanosheets were used, respectively, as semiconducting channels and gate dielectric layers in FET (field

emission transistor) devices.¹ Gigantic magneto-optical effects were observed in multilayer assemblies of two-dimensional $\text{Ti}_{0.8}\text{Co}_{0.2}\text{O}_2$ and $\text{Ti}_{0.6}\text{Fe}_{0.4}\text{O}_2$ nanosheets.¹¹

One of the most exciting new applications for metal oxides is thermoelectrics. Thermoelectric oxides are chemically and thermally stable. They can be composed of nontoxic, light, cheap, and naturally abundant elements. They can be produced through environmentally friendly means, and are expected to play a vital role in extensive applications for waste heat recovery under atmospheric conditions.¹² Most work on thermoelectric oxides has been devoted to bulk single crystals and polycrystalline samples. Very little work has been pursued for nanocrystalline oxide thermoelectrics, except for thin films on substrates.¹³ Scaling these materials to nanoscale dimensions ($<100\ \text{nm}$) offers additional control, such as decreasing the phonon thermal conductivity by phonon confinement,¹⁴ which is an effective means of increasing thermoelectric figure of merit (ZT).

Recently, the complex metal oxide Na_xCoO_2 has been vigorously researched due to its potential in thermoelectric energy harvesting.^{15,16} Na_xCoO_2 is composed of two-dimensional triangular CoO_2 layers with Na^+ intercalated between the layers, occupying a variety of possible sites.^{17,18} The $x = 0.7$ phase ($\text{Na}_{0.7}\text{CoO}_2$) is a surprisingly good thermoelectric material with metallic conductivity ($200\ \mu\Omega\cdot\text{cm}$ at 300 K), a large Seebeck Coefficient ($100\ \mu\text{V K}^{-1}$ at 300 K), and a thermoelectric power factor as high as the industry standard Bi_2Te_3 .^{15,19} Scaling Na_xCoO_2 to nanometre sizes will allow this important energy material to be optimized through size-dependent property engineering.

Cornell University, Materials Science and Engineering Department, 214 Bard Hall, Ithaca, NY, 14853, USA. E-mail: rdr82@cornell.edu

† Electronic supplementary information (ESI) available: Additional SEM images of the nanosheets, powder XRD for all intermediate and final products, a figure for the analysis of the anisotropic growth of the nanosheets, figures for further discussion regarding the synchrotron X-ray analysis, statistical information regarding nanosheet thickness, optical microscopy and TEM images of exfoliated nanosheets. See DOI: 10.1039/c2jm15550h

Chemical exfoliation of bulk materials has been the most common method to produce oxide nanosheets,^{1,3} and is responsible for the majority of exiting advances in this field. Unfortunately, this aggressive top-down chemical process can damage or alter the starting compound. For instance, chemical exfoliation of thermoelectric Na_xCoO_2 layers yields CoO nanosheets,²⁰ which are non-metallic and not useful thermoelectric materials. Chemical exfoliation techniques, which delaminate layers from bulk samples, generally produce a low yield of sheets with short lateral lengths (typically $<10\ \mu\text{m}$).³

In this work, a scalable nanomanufacturing technique for batch fabrication of 2D Na_xCoO_2 nanosheets is reported. The method is based on sol–gel chemistry and kinetic-demixing. This bottom-up synthesis is capable of producing tens of thousands of well-defined nanosheets stacked into a macro-sized pellet, providing an efficient means of large-scale crystal growth as compared to conventional nanofabrication and crystal growth techniques. The nanosheets are uniform in length and shape with high aspect ratios of nanometre thickness and millimetre lateral lengths ($10^{-5}:1$). They are readily delaminated into free-standing nanosheets without changing crystal structure.

Our method of producing millimetre length 2D nanosheets of $\text{Na}_{0.7}\text{CoO}_2$ will facilitate this important material for the nanosize property enhancements in potential thermoelectric devices. Scaling Na_xCoO_2 to nanometre dimensions is expected to significantly improve its thermoelectric performance due to phonon scattering-confinement effects.¹⁴ Phonon scattering-confinement by the nanometre dimensions is expected to reduce the thermal conductivity of $\text{Na}_{0.7}\text{CoO}_2$, which should result in enhanced ZT. In addition, due to the millimetre scale lateral lengths, the Na_xCoO_2 nanosheets can be readily applied to practical macroscopic thermoelectric devices.

Experimental

Synthesis of $\text{Na}_{0.7}\text{CoO}_2$ nanosheets

An aqueous solution is prepared at room temperature by mixing appropriate quantities of poly(acrylic acid) (PAA, average molecular weight: $M_w \sim 1800$), cobalt(II) nitrate hexahydrate (0.230 M) and sodium nitrate (0.165 M) in de-ionized water. The Na to Co ratio is set to 0.72. The ratio of PAA carboxylate groups to total metal ions is 1 : 2. The solution is stirred and evaporated at 150 °C on a hotplate until it reached 20% of the initial volume. The resulting dark red solution is then auto-combusted at 500 °C. The resulting black powder is uni-axially pressed into pellets with a rectangular die set at 400 MPa. A typical size of the pellet is 10x6x5 mm (LxWxT). The pellet is kinetically-demixed at $<300\ \text{°C}$ with a constant-current electrical field of 500 mA through Cu plates and contacts made of silver epoxy. Over the course of 48 h the voltage fluctuates between 20 V and 5 V, and decreases towards the end of the process. During the kinetic-demixing process, a red emitting current pathway appears on the pellet with temporally changing position. After the kinetic-demixing, the pellet separates into Na-rich and Na-depleted regions and the boundary between the two regions is clearly distinguishable. The Na-depleted region is mechanically weak, porous and grey while the Na-rich region is mechanically strong, dense and black. The Na-rich region of the pellet is

separated and calcined in a tube furnace to finally obtain Na_xCoO_2 nanosheets. The furnace is rapidly heated to 1030 °C and held for 15 min. The temperature is then ramped down to 1000 °C in 1.5 h and down to room temperature in the following 3 h. After calcination, Na_xCoO_2 phases have high Na content ($0.8 < x < 0.93$). To obtain the thermoelectric phase ($\text{Na}_{0.7}\text{CoO}_2$) the sample is subjected to a secondary heat treatment at 850 °C for ~ 30 h.

Exfoliation of the nanosheets

Exfoliation of the $\text{Na}_{0.7}\text{CoO}_2$ nanosheets is accomplished through thermal shock and ultrasonication. Pellets of stacked Na_xCoO_2 nanosheets are repeatedly quenched from 500 °C in clean (18 M Ω), room temperature water, followed by a brief sonication in water. The nanosheets are then collected from the water surface.

XRD, SEM, EDS and TEM characterization

All of the intermediate and final products of the synthesis procedure were examined by a high resolution ($\sim 1\ \text{nm}$ at 2 keV) scanning electron microscope (SEM, LEO 1550 FESEM) and by X-ray diffraction (XRD). At least 100 nanosheets were measured by SEM for nanosheet thickness statistical analysis. SEM-EDS (Energy Dispersive X-ray Spectroscopy) was performed for compositional analysis. Conventional 2θ – θ XRD measurements were conducted using a Scintag (Pad-X) with a Cu-K α 1 source. The samples were finely ground before the XRD based phase analysis measurements in order to minimize possible texturing and crystal alignment effects. The measured XRD peak locations were identical to those of un-ground samples. Transmission Electron Microscopy (TEM), dark field imaging, and electron diffraction were performed with an FEI T12 Twin TEM.

Synchrotron X-ray analysis

To effectively characterize the obtained stacked nanosheet structures a 6-axis diffractometer at Cornell High Energy Synchrotron Source (CHESS) was used. The independent 6-axis allows for 2D scans in reciprocal space which can be arranged to obtain reciprocal lattice mapping, rocking curve, and combinations of these two.²¹ The nanosheets were oriented with their [001] axis aligned vertically, and the incident beam skimmed the horizontal plane ($\sim 0.05^\circ$). A linear detector (represented by Δ axis in angular space) was fixed to a position defined with respect to the Bragg Condition of {101} planes of $\text{Na}_{0.7}\text{CoO}_2$ and aligned parallel to [001]. During the measurements, the sample was rotated about [001] (φ rotational axis). This measurement method simultaneously provided a rocking curve type scan for (100) planes due to the φ rotation and a θ – 2θ type of scan for (001) planes due to the linear range of the detector. Additional details of this process are provided in Fig. S5 and S6 in the Electronic Supplementary Information†.

Results and discussion

SEM images of the metal oxide nanosheets are shown in Fig. 1. The nanosheets lengths are millimetres (Fig. 1e and Fig. S1, ESI†, show two different $\sim 1.8\ \text{mm}$ -long stacks of nanosheets),

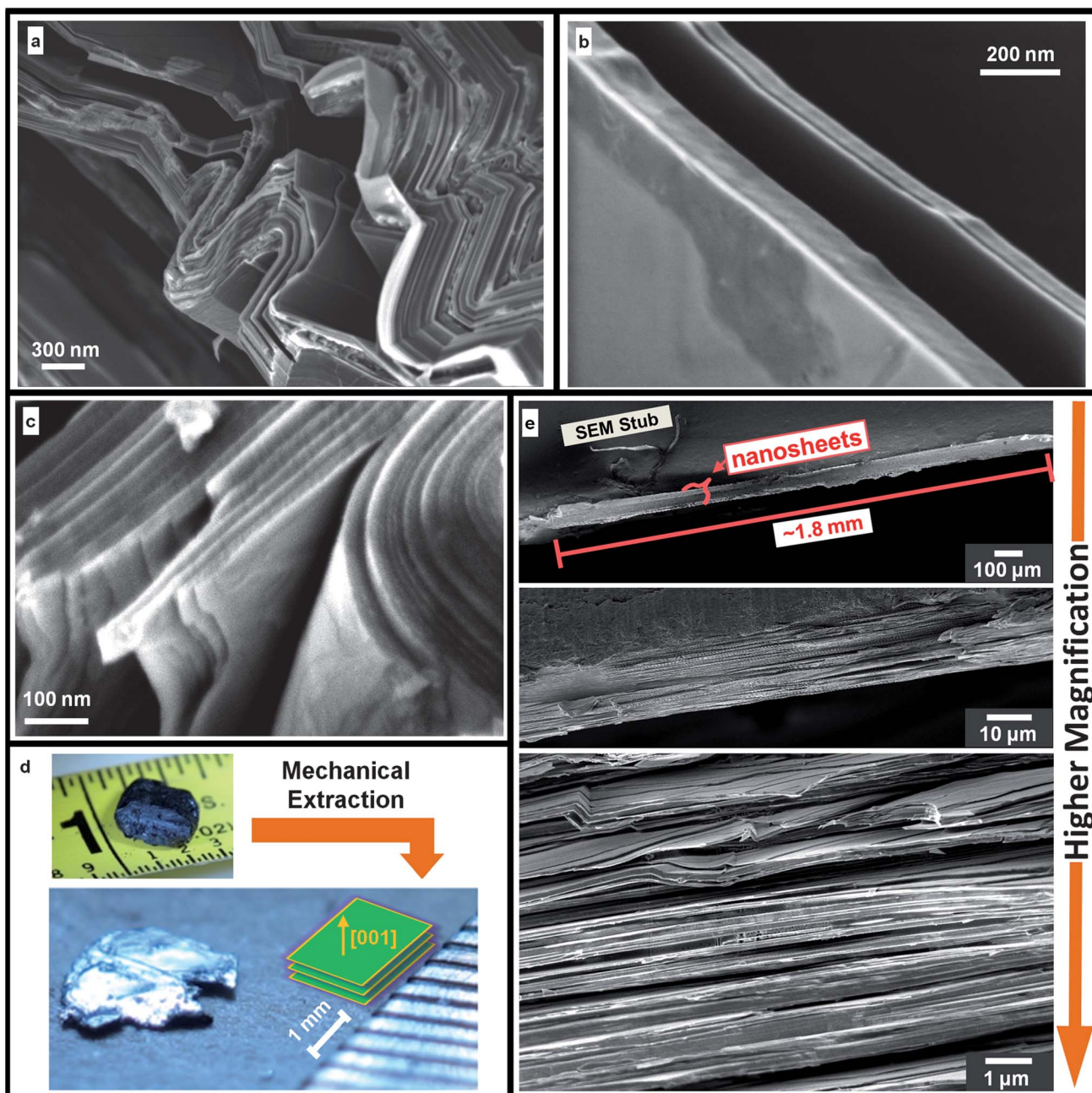


Fig. 1 SEM and optical microscope images of metal oxide nanosheets: (a) SEM image of metal oxide nanosheets displaying extreme ductility after mechanical bending is applied. (b) SEM image of two individual nanosheets of $\text{Na}_{0.7}\text{CoO}_2$ showing thicknesses of $\sim 50\text{--}100$ nm. (c) SEM image of the nanosheets showing the typical nanosheet thickness profile (18.2 nm in average, see Fig. S2, ESI †). (d)(top) Optical image of the bulk pellet product consisting of thousands of stacked nanosheets and (bottom) a single nanosheet stack obtained by mechanical extraction. The inset drawing shows the alignment of the nanosheets in the nanosheet stack. (e) SEM images of nanosheet stacks from low magnification (top) to high magnification (bottom). Total nanosheet length is 1.8 millimetres, and stack thickness is nominally 100 microns.

can be easily bent (Fig. 1a), and have a smooth surface (Fig. 1b). According to the statistical analysis performed by SEM, the nanosheet thickness is 18.2 nm in average (Fig. 1c and Fig. S2, ESI †). The nanosheets are produced as stacks of sheets (Fig. 1e) that can number in the tens to hundreds of thousands of nanosheets, per stack. Optical images of the bulk product are shown in Fig. 1d, along with the extraction of a stack of nanosheets.

The synthetic procedure for our Na_xCoO_2 nanosheets consists of a) the Pechini-method coordination of metal ions, b) pyrolysis

into oxide flakes, c) pressurized pellet formation, d) electric-field (E-field) induced kinetic-demixing, and e) calcination (Fig. 2).

Our sol-gel synthesis employs the Pechini method where metal precursors are dissolved in an appropriate solvent by an organic complexing agent, and the resulting homogenous liquid solution is evaporated into a viscous resin intermediate.²² The resin is then heated to autocombustion. The organic components are pyrolyzed in this process, and the resulting product is a uniform metal oxide mixture. The molar ratio between the different metal

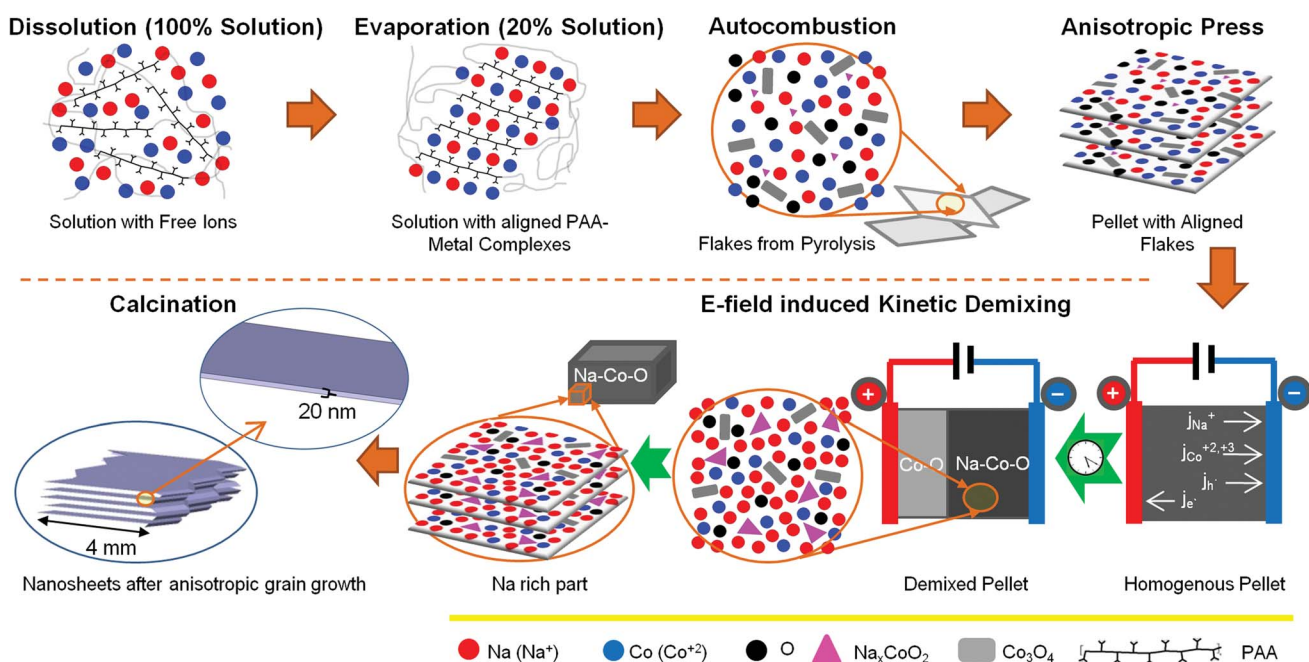


Fig. 2 Schematic diagram for the synthesis procedure for millimetre-length 2D Na_xCoO_2 nanosheets: Metal precursors and PAA are dissolved in water. The solution is evaporated to eighty-percent of its initial volume, leading to metal complex formation. The viscous liquid is autocombusted into a pyrolyzed phase, which form as flakes. The pyrolyzed flakes are uniaxially pressed into a rectangular pellet. Electric field is applied to the pellet, and kinetic-demixing occurs due to the different mobility of Na and Co atoms. The Na-rich region is calcined at 1030 °C leading to the formation of the nano-layered structure due to anisotropic grain growth.

cations in the starting solution is maintained in the oxide mixture.²² By proper choice of the solvent, organic complexing agent and metal precursors in the liquid solution, the atomic homogeneity can be maintained in the metal oxide autocombusted product.²³ In this work, the Pechini method is modified to entrap the metal ions in solutions by using poly(acrylic acid) as the chelating agent. The metal cations are expected to be stabilized by the chelating groups on the ligand, through dipole forces between water molecules and metal ions, and by the crosslinking and physical tangling of polymer chains which can trap both the cations and solvents in a drying polymer-metal ion complex sheet, termed “polymeric entrapment” or “steric entrapment”.^{24,25} This polymer-metal ion complex sheet is not to be confused by either atomic layering of Na_xCoO_2 or the 2D Na_xCoO_2 crystals reported in this work. The crosslinking is likely to occur bi-axially which causes parallel alignment of PAA-metal complexes, similar to that reported for alginate.²⁶ The structure of these polymeric entrapped layers is evident after the solution is pyrolyzed. SEM images show <200 nm thick and <400 μm long autocombusted flakes which include Co_3O_4 crystals with a relatively minor amount of CoO according to the X-ray diffraction analysis (XRD) (Fig. 3a and Fig. S3, ESI†). Additionally, edge-to-edge-connected plate-like particles form after the calcination of the autocombusted powder (650 °C, 1 h) (Fig. 3b). Similar behavior was observed by Zhang *et al.*²⁷ for alginate gel based synthesis of tiled $\text{Na}_x\text{Co}_2\text{O}_4$ crystals. The entrapment and crosslinking by PAA is crucial for forming the autocombusted flakes: if citric acid is used in place of PAA and the ratio of carboxylic moieties to the number of metal cations is fixed (2 : 1), flake-like formations do not occur after autocombustion and the volume of the autocombusted form is much

smaller compared to the case with PAA (*i.e.*, less than 1/3). Similarly, flake-like formations do not form when the ratio of PAA coordination sites to metal cations is varied from the critical value of 2. When the ratio is 1 (one carboxylic site to one metal cation) an explosive combustion occurs, and the process does not produce flake-like formations. When the number of carboxylic sites exceed the number of metal cations (*i.e.*, ratio of 3 or 4), the autocombustion is slower, the volume expansion during the autocombustion is significantly reduced and flake-like formations are not produced.

After the autocombusted flakes are pressurized by a rectangular die, XRD results show that (1) the cobalt oxide phases formed during the autocombustion are still present, and (2) the emergence of a Na_xCoO_2 phase (Fig. S3, ESI†). Similar to the autocombusted product, the pressurized pellet includes Co_3O_4 crystals with relatively minor amount of CoO. However, after the pressurization process a distinct and relatively low intensity peak appears which matches with $\text{Na}_{0.6}\text{CoO}_2$ phase (Fig. S3, ESI†). All of the peak intensities for both the autocombusted flakes and the pressurized pellet XRD were low which can be an indication of partially amorphous structure.

The next step, kinetic-demixing, is the critical component to forming millimetre-length nanosheets. After application of a 500 mA current and a 1030 °C calcination, the nanosheet lateral lengths can reach ~1.8 millimetres. Samples with identical processing conditions, but *without* kinetic-demixing, reach only up to ~200 μm , *i.e.*, nine-times shorter. The alignment of the pressurized flakes has an influence on the kinetic-demixing: E-field induced kinetic-demixing is only possible perpendicular to the pressure axis. When an E-field is applied parallel to the pressure axis no current is observed (under identical voltage conditions as

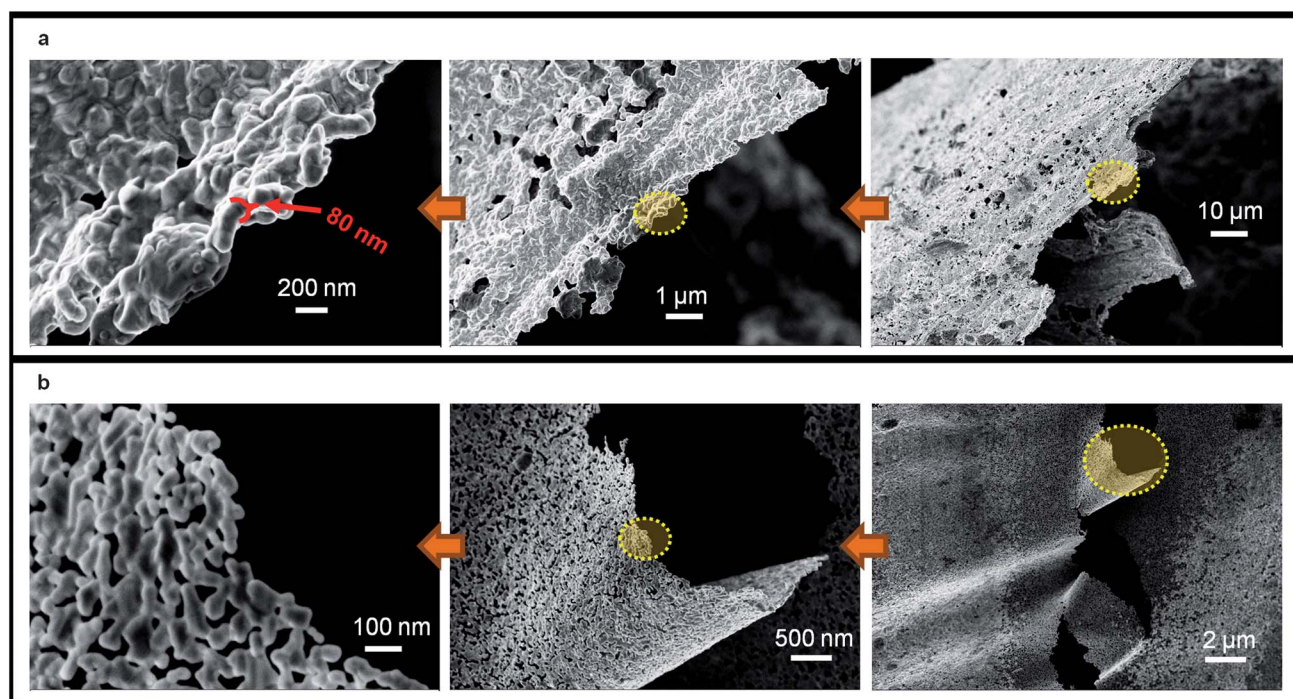


Fig. 3 (a) SEM images of the flakes that appear after the autocombustion of the PAA-Metal Complex aqueous solution. The thickness of the flakes is <200 nm and the length measures up to 400 μm . (b) SEM images of the edge-to-edge-connected Na_xCoO_2 crystals that appear after the low temperature calcination (650 $^\circ\text{C}$) of the autocombusted form. SEM images are sorted from high magnification to low magnification (left to right). The magnified regions are circled in the low magnification images.

the perpendicular arrangement). This directional limitation on the E-field induced kinetic-demixing is likely a result of the lateral alignment of the autocombusted flakes after the uni-axial pressure process; the flakes provide a more contiguous pathway for the current than a cross-plane pathway provides.

After the application of the E-field to the homogenous pellet, an abrupt transition in Na concentration is observed along the E-field application axis and, according to XRD results, new phases form in the Na-rich part of the pellet. Elemental analysis from an SEM-EDS (Energy Dispersive X-ray Spectroscopy) line scan shows the abrupt transition in Na content and morphology between the sample regions adjacent to the cathode and that to the anode (Fig. 4). The region near the anode is Na-depleted and extremely porous while the material near the cathode is Na-rich and has a smooth unbroken surface (Fig. 4a inset images). According to the XRD results, the Na-deficient region is composed of only Co_3O_4 crystals while the Na-rich region includes Na-Co-O based stoichiometric phases such as $\text{Na}_{0.6}\text{CoO}_2$, Na_4CoO_3 and Na_4CoO_4 in addition to Co_3O_4 (Fig.S3, ESI†).

Oxygen is a necessary component of the kinetic-demixing to form nanosheets. When the kinetic-demixing is performed under nitrogen gas, the abrupt Na concentration change and the formation of the porous region were diminished to a negligible level compared to when kinetic-demixing is performed under atmospheric conditions. As a comparison, when the kinetic-demixing is performed under nitrogen gas the volume of the Na-deficient region is $\sim 5\%$ of the initial pellet volume, whereas, for the same demixing time and applied current, if the

kinetic-demixing is performed under atmospheric conditions the volume of the Na-deficient region is $\sim 45\%$ (Fig. 5).

During the E-field induced kinetic-demixing process Co ions are expected to have significantly lower mobility compared to Na ions due to the low temperatures in our process ($<300\text{ }^\circ\text{C}$). Extrapolating from previous work on the Co-O system results in extremely low Co tracer diffusion coefficients at temperatures below 300 $^\circ\text{C}$ (i.e., $D_{\text{Co}}^* = D_{\text{Co}}^{*0} \cdot e^{(-E_{\text{Co}}/RT)}$ with $D_{\text{Co}}^{*0} = 1.52 \times 10^{-2} \text{ cm}^2 \text{ s}^{-1}$ and $E_{\text{Co}} = 172400 \text{ J mol}^{-1}$; $D_{\text{Co}}^* \approx 3 \times 10^{-18} \text{ cm}^2 \text{ s}^{-1}$ at 300 $^\circ\text{C}$).²⁸ Additionally, Ohta *et al.* reported that Co ions were stationary even at higher temperatures (600–700 $^\circ\text{C}$) during reactive solid-phase epitaxial growth of Na_xCoO_2 via lateral diffusion of Na into a cobalt oxide film from NaHCO_3 powder.²⁹

The movement of Na and Co ions and the pore formation near the cathode can be best explained by E-field induced kinetic-demixing of multicomponent oxide mixtures. According to Martin's description of E-field induced kinetic-demixing of an initially homogenous multicomponent metal oxide mixture,³⁰ the cations move towards the cathode due to the electrochemical driving force exerted by the E-field. The cations in such multicomponent oxides, however, don't move as free ions since this usually requires an extremely high amount of energy to liberate the cation from O^{2-} (e.g., formation enthalpies of CoO and Co_3O_4 : $\Delta_f H_{\text{CoO}}^0 = -237.735 \text{ kJ mol}^{-1}$ and $\Delta_f H_{\text{Co}_3\text{O}_4}^0 = -910.020 \text{ kJ mol}^{-1}$).³¹ They instead move by forming new metal oxides at the cathode and by decomposing existing metal oxides at anode. At the cathode, the cations are involved in the chemical reaction described in eqn (1) (for a cation of $\alpha+$ oxidation state):³⁰

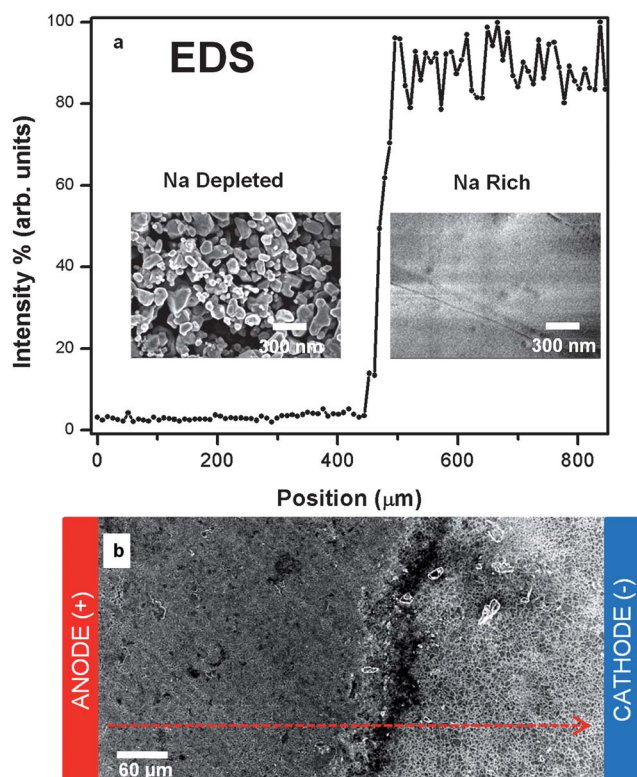
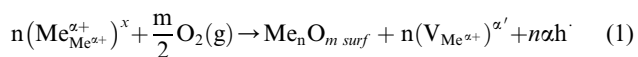


Fig. 4 The effect of kinetic-demixing. (a) Na concentration from EDS line scan of the pellet after kinetic-demixing with respective SEM images of the Na depleted and Na-rich regions. A stark contrast is seen between these regions: the Na depleted regions are more porous and contain nano-grains while the surface of the Na-rich region is smooth. (b) SEM image showing cracking between the two regions. The separation line corresponds to the abrupt jump shown in the EDS of (a). Red dashed arrow shows direction of EDS scan.



In this equation Me represents a metal, V represents vacancy, h represents hole, the *surf* subscript refers to the surface at the electrode and the superscripts α' , and x represent $-\alpha$, +1 and 0 charges respectively according to the Kröger-Vink notation. This expression conveys the following process: n metal ion(s) in the metal oxide compound (*i.e.* Me_nO_m) reacts with atmospheric oxygen and forms a new metal oxide at the electrode surface (*i.e.* $\text{Me}_n\text{O}_{m \text{ surf}}$) leaving behind n metal ion vacancy(ies), and n · α free hole(s) are generated to compensate the charge. Here the metal ion can be either one of the metal cations (Na or Co in our case) in the multicomponent oxide mixture. The same chemical reaction described by eqn (1) is reversed at the anode side.³⁰ As a result of the reaction described by eqn (1), the oxygen sublattice (formed at the cathode as the new metal oxide such as Na–O, Co–O and/or Na–Co–O stoichiometric compounds) moves towards the anode. The movement of cations, then, is relative to the movement of the oxygen sublattice (analogous to a boat advancing against the flow of a river). The same reaction also generates vacancies at the cathode and terminates them at the anode, which results in a vacancy flow towards anode (see eqn (1)). If the mobilities of the two cations are sufficiently different, the high and low mobility cations will separate from this reaction

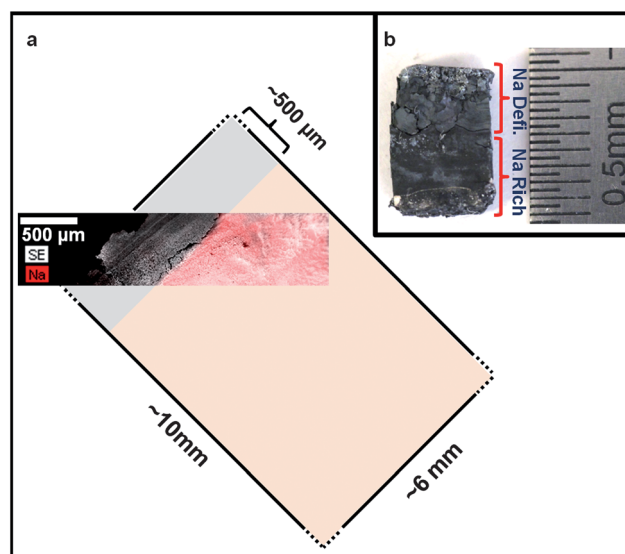


Fig. 5 Na-deficient and Na-rich regions after E-field induced kinetic-demixing performed under nitrogen gas (a) and atmospheric conditions (b). (a) An SEM image with secondary-electron EDS mapping for Na – shown in red – for a sample pellet demixed under nitrogen gas. The black outer lines mark the approximate boundaries of the full pellet. The SEM rectangle shows the false-color mapping for Na in red, and the SEM image position relative to the full pellet. The Na-deficient region is only ~5% of the total volume, indicating that very little kinetic-demixing occurred. (b) Optical image of the pellet which is demixed under atmospheric conditions. Under these conditions 45% of the pellet is now Na-deficient.

process: the higher mobility cations will fill the newly generated vacancies – due to their high jump frequency – and the lower mobility cations will fill the vacancies emptied by higher mobility cations. As a result, the cation with a higher diffusion coefficient concentrates near the cathode whereas the lower diffusion coefficient cation concentrates near the anode.³⁰

In Martin's description of kinetic-demixing, atmospheric oxygen is necessary for the movement of cations, as is evident in the reaction described by eqn (1).³⁰ Our results showing a lack of demixing when performed under nitrogen gas confirm a similar mechanism: Na ions require oxygen to move (demix) through our samples. In this work, the mobility of the Co ions is expected to be much lower than the mobility of Na ions. Therefore newly forming vacancies are filled mostly by Na ions, and different from Martin's observations,³⁰ in the limited demixing time, the lower mobility Co ions can't fill all of the vacancies created by the movement of Na ions toward the cathode. After the Na ions move from the anode region a porous material develops because Co ions are unable to fill these vacancies.

The kinetic-demixing creates an Na saturated compound, which increases the Co diffusion coefficient during the high temperature (1030 °C) calcination, leading to the millimetre-length nanosheets. Correlating the EDS data with the sample volume suggests that the Na:Co ratio can be as high as 1.3 in the Na-rich side which is ~2x higher than the most thermodynamically stable phase of Na_xCoO_2 .³² During the high temperature (1030 °C) calcination, this Na rich part of the pellet shows molten fluidity that is evident from the pellet shape deformation (*i.e.*

rectangular form to semi-spherical form) after the calcination. However, such shape deformation is not observed for the samples calcined directly after pressure application without the kinetic-demixing process (*i.e.*, when the Na:Co ratio is maintained at 0.71). The fluidity in the Na saturated compound at high temperatures is associated with a significant increase in the Co diffusion coefficient. The increased Co mobility is in contrast to its very low mobility in the kinetic-demixing process, which is performed at low temperatures (<300 °C). Assuming the dominant diffusion mechanism is cation vacancy diffusion, this increase in the Co diffusion coefficient can be explained by the temperature dependence of Co diffusion coefficient and also the “physical correlation effect”³³ between the Co and Na atomic motions. A previous study from Schnehage *et al.* on the $\text{Co}_x\text{Mg}_{1-x}\text{O}$ system ($0 \leq x \leq 1$) found the Co tracer diffusion coefficient increases $\sim 10^9$ times in pure CoO when the temperature increased from 300 °C ($D_{\text{Co}}^* \approx 3 \times 10^{-18} \text{ cm}^2 \text{ s}^{-1}$) to 1030 °C ($D_{\text{Co}}^* \approx 2 \times 10^{-9} \text{ cm}^2 \text{ s}^{-1}$).²⁸ According to the same work, the diffusion coefficient of the low mobility Mg atoms can be increased up to ~ 500 times by mixing with the highly mobile Co atoms due to the “physical correlation” between the movements of the two atomic species (D_{Mg}^* increases with increasing x). Here “physical correlation” refers to a deviation from the directional randomness in atom/vacancy jumps due to the difference in the intrinsic jump frequencies of different atomic species.³³ In the current work the Co ions are the low mobility species and the Na ions are the high mobility species, as is evidenced in the kinetic-demixing process. The diffusion coefficient of the Co cations will therefore be amplified by two factors: 1) the temperature increase and 2) from the “physical correlation” of their mixing with the highly mobile Na ions. Our observation that high temperature molten fluidity exists only kinetically-demixed samples (*i.e.*, if the samples were not kinetically-demixed then there was no molten fluidity) points to increased diffusion from the physical correlation of a larger Na:Co ratio. The Co diffusion amplification significantly reduces kinetic limitations, and leads to long nanosheet formation through cooperative effects including: facile grain growth, fluidity in the pellet during calcination, and enhancement of the anisotropic growth along the (001) plane. The growth along the (001) plane is naturally favored due to the high difference in surface energies between the (001) plane and the planes perpendicular to (001), which originates from the highly different bond energies along corresponding directions.³⁴

Anisotropic grain growth behavior of kinetically-demixed samples was analyzed comparing them with non-kinetically-demixed samples at several calcination temperatures (650 to 1030 °C, Fig. S4, ESI†). For both kinetically-demixed and non-kinetically-demixed samples the nanosheet *thickness* does not change with calcination temperature, but the nanosheet *length* increases with increasing calcination temperature. The nanosheet lengths are similar for the kinetically demixed and non-kinetically-demixed samples at 650 °C, 750 °C and 850 °C (*i.e.*, $\sim 1 \mu\text{m}$, $\sim 5 \mu\text{m}$ and $\sim 13 \mu\text{m}$ respectively). However, at temperatures higher than 950 °C the nanosheets for the kinetically-demixed samples become significantly longer compared to non-kinetically-demixed samples. Nanosheets resulting from kinetic-demixed samples with calcination at 950 °C (the fluidity of the pellet is not observed at this temperature) are ~ 4 times longer than the non-kinetically-demixed samples. At 1030 °C, the nanosheets

resulting from the kinetically-demixed samples are ~ 9 times longer than the nanosheets resulting from the non-kinetically-demixed samples. The nanosheet length can be as long as 1.8 mm for the kinetically-demixed samples calcined at 1030 °C.

The θ -2 θ XRD study of the crushed powders after calcination indicates trigonal $\text{Na}_{0.9}\text{CoO}_2$ ¹⁸ as the dominant phase. This phase can be transformed to the hexagonal $\text{Na}_{0.7}\text{CoO}_2$ ¹⁷ phase after a secondary heat treatment (875 °C–30 h) (Fig. S3, ESI†).³⁵ The transition from $x = 0.9$ to 0.7 has no effect on nanosheet thickness and length. θ -2 θ XRD scans show only the 00L and 104 peaks for the millimetre-long nanosheets aligned parallel to the sample stage, while other diffraction peaks are absent (Fig. 6a). This result indicates that the nanosheets are large crystals which are strongly oriented.

Conventional θ -2 θ XRD scans of the 2D crystals show no finite size broadening of the 00L peaks (Fig. 6a). The 6-angle diffractometer based XRD analysis conducted at the Cornell High Energy Synchrotron Source (CHESS) provides a more accurate description of the 2D crystals and finite-size effects (see Fig. S5, ESI†). Results from this XRD analysis show that the crystal symmetry is consistent with $\text{Na}_{0.7}\text{CoO}_2$. Peaks at $\sim 7.5^\circ$ from the horizontal (Δ) and separated by 60° along the in-plane ϕ axis correspond to the six-fold symmetry of the (101) planes of $\text{Na}_{0.7}\text{CoO}_2$ (Fig. 6b). Higher resolution scans of these peaks from several samples show ~ 4 –12 diffraction spots within $\sim 1^\circ$ along the ϕ axis. Fig. 6c shows the case with ~ 12 diffraction spots. Because the ϕ scan represents a rocking curve for (100) planes, these spots are the result of rotational misalignment ($\sim 0.1^\circ$ with respect to each other) of the ~ 12 distinct crystals around [001].

The CHESS diffraction results also show peak broadening associated with the 2D crystal thickness (Fig. 6b and 6c). Finite-size broadening effects can be analyzed by examining the (101) diffraction. Since the Δ and ϕ axes are orthogonal in both real and reciprocal space, and Δ axis projects onto the vertical linear detector which is parallel to [001], vertical broadening of the 101 peak corresponds to finite size effects along the [001] direction (see Fig. S6c, ESI†). According to Scherrer analysis (Fig. 6d), the broadening along the Δ axis gives an average nanosheet thickness of 19.1 nm, which is in good agreement with statistical analysis performed by SEM (18.2 nm, Fig. S2, ESI†). It is surprising that finite size broadening is only observed in the high-resolution 2D scan, but not in conventional θ -2 θ XRD of (001) planes. The likely explanation why broadening is not observed for the conventional θ -2 θ XRD is because the nanosheets are stacked in registry along [001]. Broadening is observed in the in-plane 2D scans of the (101) peak because these planes are not contiguous between nanosheets, and thus we are able to tease out the finite size of the nanosheets along [001]. Such stacking of nanosheets is referred to as “turbostratic” arrangement of the 2D crystals (planes rotated around the c -axis, see Fig. S6b, ESI†).³⁶ Presence of this arrangement is substantiated by the rotational misalignment of the ~ 12 grains (Fig. 6c).

The two distinct diffraction spots observed along Δ axis indicate two different (100) lattice spacings. A hypothetical 3D sketch of the possible 2D crystal stacking configuration is provided in Fig. 6e. It is important to note that no broadening was observed for either of the two (100) d-spacings. This observation confirms that the finite size along [001] solely originates from the nanosheet thickness.

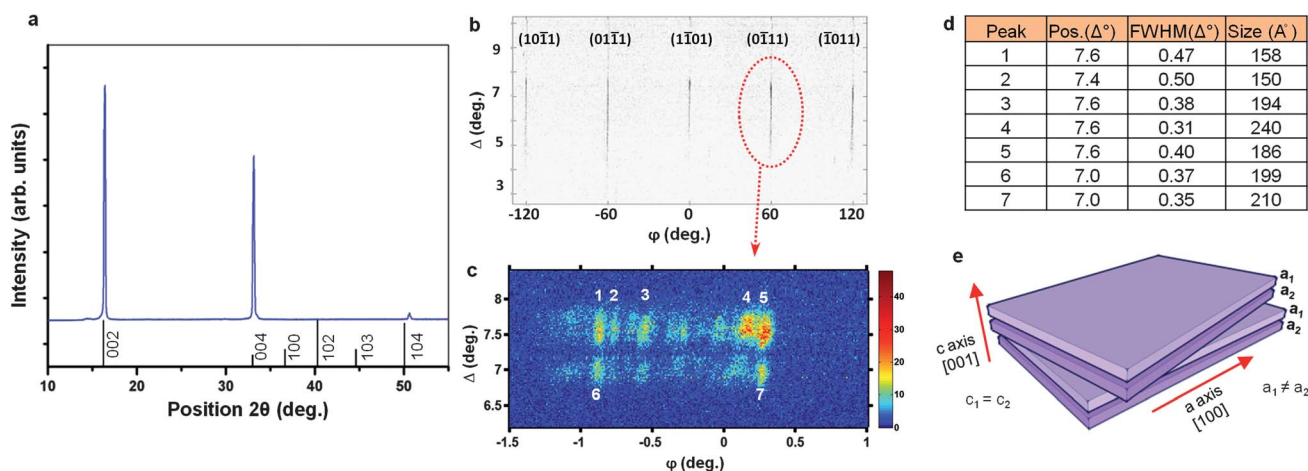


Fig. 6 X-ray characterization of nanosheets. (a) Conventional θ - 2θ XRD of $\text{Na}_{0.7}\text{CoO}_2$ nanosheets aligned parallel to sample stage (stick lines correspond to JCPDS PDF card file #00-030-1182). (b) Grazing incidence diffraction from hexagonal $\{10\bar{1}0\}$ planes of $\text{Na}_{0.7}\text{CoO}_2$ nanosheets (ϕ scan with linear detector around 101 peak) indicates 6-fold symmetry with peaks around 7.5° (Δ) located 60° (ϕ) away from each other. (c) Higher resolution of the region in (b) with the seven most distinct diffraction spots numbered. (d) Finite sizes calculated using Scherrer's equation for the seven spots in (c). (e) 3D Sketch of a hypothetical ordering of nanosheets according to available diffraction data.

Extremely large $\text{Na}_{0.7}\text{CoO}_2$ nanosheets are exfoliated from the bulk, stacked nanosheet samples and their crystal properties are characterized. Free-standing exfoliated 2D crystals are typically 10–350 microns wide, as characterized using optical and transmission electron microscopy (Fig. 7 and Fig. S7, ESI[†]). This length (350 microns) yields an order of magnitude improvement in the maximum lateral lengths of typical metal oxide 2D crystals

(nanosheets).³ The exfoliated pieces are estimated to be between 20–100 nm thick based on layer counting at the sample edges (Fig. S8, ESI[†]). Selected area electron diffraction (SAED) from multiple regions of each 2D crystal confirm the hexagonal crystal symmetry and lattice spacing of $\text{Na}_{0.7}\text{CoO}_2$ with $[001]$ being the zone axis. The well-defined points in SAED (Fig. 7a) confirm that the stacked nanosheets are in registry with one another

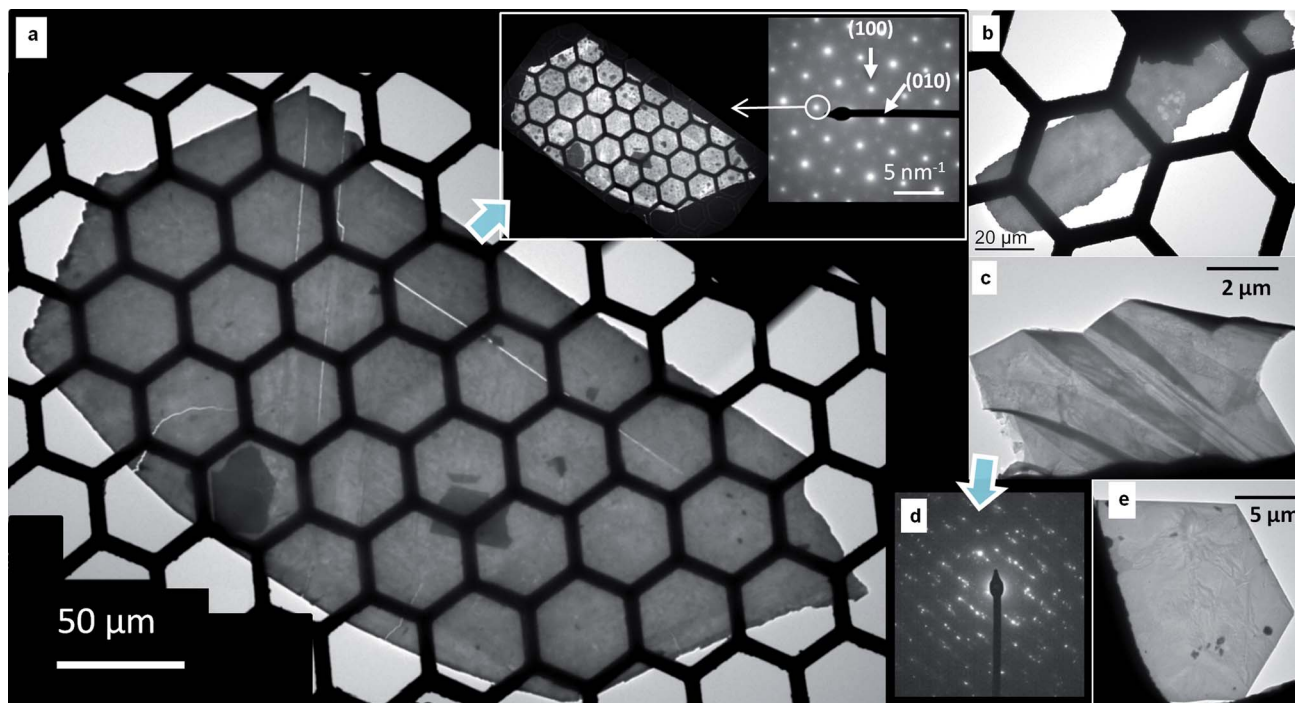


Fig. 7 TEM images of nanosheets of $\text{Na}_{0.7}\text{CoO}_2$. (a) $350\ \mu\text{m} \times 150\ \mu\text{m} \times 100\ \text{nm}$ thick sheet composed of ~ 5 individual nanosheets. Image was compiled from 3 electron micrographs. Inset: ED pattern confirming nanosheets are aligned, single crystal and the orientation of cross-plane thickness is $[001]$. Dark-field imaging confirms that this ED pattern is representative of the entire sheet and that the sheet is a single crystal. (b) $120\ \mu\text{m} \times 25\ \mu\text{m} \times 100\ \text{nm}$ thick nanosheet as another example of large scale exfoliation (c) Image of folded sheet and (d) corresponding ED pattern. (e) Micron sized sheet with hexagonal growth morphology matching unit cell.

along the c-direction. TEM dark-field analysis from a hexagonal-lattice {100} diffraction spot shows the entire sheet illuminated for the exfoliated nanosheets, proving that the entire sheet is a single crystal (Fig. 7a inset). In reflected white light (Fig. S7a, ESI†) the nanosheets appear opaque and black, consistent with bulk samples of Na_{0.7}CoO₂. However, under transmitted light they range from a translucent yellow to red (Fig. S7b, ESI†). This finding yields a facile method to distinguish between thin, electron transparent layers and bulk pieces of Na_{0.7}CoO₂. Cross-polarized transmitted light shows the sheets to be optically isotropic. This observation is expected when viewing a hexagonal crystal along [001].

Conclusions

A novel synthesis has been developed for production of millimetre-length nanosheets of Na_xCoO₂. Our nanomanufacturing method is scalable and low-cost, capable of producing tens of thousands of nanosheets for device integration. The nanosheets have thicknesses in the tens of nanometres while their lateral lengths are millimetres, resulting in a very high anisotropic aspect ratio (10⁻⁵:1:1). Synchrotron X-ray studies indicated that the nanosheets are turbostratically stacked within the pellets. The nanosheets are readily exfoliated into free-standing sheets reaching 350 microns in length with thicknesses ranging ~20–100 nm. Selected area electron diffraction studies indicated that the crystal properties are maintained after the exfoliation process. This new nanomanufacturing method can be applicable to other atomically layered oxides.

Acknowledgements

We thank Dr Arthur Woll for his valuable assistance with the CHESS measurements and analysis, Prof. Rüdiger Dieckmann for beneficial discussions on the kinetic-demixing process and Prof. Bruce van Dover for equipment use. We also thank Dr Mahmut F. Aksit for his help. We also acknowledge support of Cornell Center for Materials Research (CCMR) with funding from the MRSEC program of the National Science Foundation (DMR0520404), and the support of Energy Materials Center at Cornell (EMC²), an Energy Frontier Research Center funded by the U.S. Department of Energy, Office of Science, Office of Basic Energy Science under Award Number DE-SC0001086.

Notes and references

- 1 M. Osada and T. Sasaki, *J. Mater. Chem.*, 2009, **19**, 2503–2511.
- 2 J. N. Coleman, M. Lotya, A. O'Neill, S. D. Bergin, P. J. King, U. Khan, K. Young, A. Gaucher, S. De, R. J. Smith, I. V. Shvets, S. K. Arora, G. Stanton, H.-Y. Kim, K. Lee, G. T. Kim, G. S. Duesberg, T. Hallam, J. J. Boland, J. J. Wang, J. F. Donegan, J. C. Grunlan, G. Moriarty, A. Shmeliov, R. J. Nicholls, J. M. Perkins, E. M. Grievson, K. Theuwissen, D. W. McComb, P. D. Nellist and V. Nicolosi, *Science*, 2011, **331**, 568–571.
- 3 R. Ma and T. Sasaki, *Adv. Mater.*, 2010, **22**, 5082–5104.
- 4 A. Takagaki, M. Sugisawa, D. Lu, J. N. Kondo, M. Hara, K. Domen and S. Hayashi, *J. Am. Chem. Soc.*, 2003, **125**, 5479–5485.
- 5 L. Z. Wang, K. Takada, A. Kajiyama, M. Onoda, Y. Michiue, L. Q. Zhang, M. Watanabe and T. Sasaki, *Chem. Mater.*, 2003, **15**, 4508–4514.
- 6 X. T. Li Zhang and Wenbin Gao, *Cryst. Growth Des.*, 2008, **8**, 2489–2492.
- 7 W. Sugimoto, H. Iwata, Y. Yasunaga, Y. Murakami and Y. Takasu, *Angew. Chem., Int. Ed.*, 2003, **42**, 4092–4096.
- 8 S. Suzuki and M. Miyayama, *J. Phys. Chem. B*, 2006, **110**, 4731–4734.
- 9 S. Suzuki and M. Miyayama, *J. Electrochem. Soc.*, 2007, **154**, A438–A443.
- 10 H. Sato, K. Okamoto, K. Tamura, H. Yamada, K. Saruwatari, T. Kogure and A. Yamagishi, *Appl. Phys. Express*, 2008, **1**, 35001.
- 11 M. Osada, Y. Ebina, K. Takada and T. Sasaki, *Adv. Mater.*, 2006, **18**, 295–299.
- 12 K. Koumoto, Y. Wang, R. Zhang, A. Kosuga and R. Funahashi, *Annu. Rev. Mater. Res.*, 2010, **40**, 363–394.
- 13 Y. Wang, Y. Sui, P. Ren, L. Wang, X. J. Wang, W. H. Su and H. J. Fan, *Inorg. Chem.*, 2010, **49**, 3216–3223.
- 14 W. Liu and M. Asheghi, *J. Appl. Phys.*, 2005, **98**, 123523–123526.
- 15 I. Terasaki, Y. Sasago and K. Uchinokura, *Phys. Rev. B: Condens. Matter*, 1997, **56**, 12685–12687.
- 16 Y. Y. Wang, N. S. Rogado, R. J. Cava and N. P. Ong, *Nature*, 2003, **423**, 425–428.
- 17 Q. Huang, M. L. Foo, R. A. Pascal, J. W. Lynn, B. H. Toby, T. He, H. W. Zandbergen and R. J. Cava, *Phys. Rev. B*, 2004, **70**, 184110(1)–184110(7).
- 18 L. Viciu, J. W. G. Bos, H. W. Zandbergen, Q. Huang, M. L. Foo, S. Ishiwata, A. P. Ramirez, M. Lee, N. P. Ong and R. J. Cava, *Phys. Rev. B*, 2006, **73**, 174104(1)–174104(10).
- 19 I. Terasaki, I. Tsukada and Y. Iguchi, *Phys. Rev. B: Condens. Matter*, 2002, **65**, 195106.
- 20 Y. Masuda, Y. Hamada, W. S. Seo and K. Koumoto, *J. Nanosci. Nanotechnol.*, 2006, **6**, 1632–1638.
- 21 D. M. Smilgies, D. R. Blasini, S. Hotta and H. Yanagi, *J. Synchrotron Radiat.*, 2005, **12**, 807–811.
- 22 M. P. Pechini, *U.S. Patent* 3 330 697, 1967.
- 23 S. Sakka, *Handbook of sol-gel science and technology: processing, characterization and applications*, Kluwer Academic Publishers, 2005.
- 24 M. A. Gulgun, M. H. Nguyen and W. M. Kriven, *J. Am. Ceram. Soc.*, 1999, **82**, 556–560.
- 25 M. Kakihana, *J. Sol-Gel Sci. Technol.*, 1996, **6**, 7–55.
- 26 D. A. Rees and E. J. Welsh, *Angew. Chem., Int. Ed. Engl.*, 1977, **16**, 214–223.
- 27 L. Zhang, X. F. Tang and W. B. Gao, *J. Electron. Mater.*, 2009, **38**, 1229–1233.
- 28 M. Schnehage, R. Dieckmann and H. Schmalzried, *Berichte Der Bunsen-Gesellschaft-Physical Chemistry Chemical Physics*, 1982, **86**, 1061–1065.
- 29 H. Ohta, S. W. Kim, S. Ohta, K. Koumoto, M. Hirano and H. Hosono, *Cryst. Growth Des.*, 2005, **5**, 25–28.
- 30 M. Martin, *Solid State Ionics*, 2000, **136**, 331–337.
- 31 M. W. Chase, *JANAF thermochemical tables*, American Chemical Society, 1986.
- 32 Y. S. Meng, Y. Hinuma and G. Ceder, *J. Chem. Phys.*, 2008, **128**, 104708.
- 33 J. Philibert, *Atom movements: diffusion and mass transport in solids*, Éditions de Physique, 1991.
- 34 C. T. Lin, D. P. Chen, P. Lemmens, X. N. Zhang, A. Maljuk and P. X. Zhang, *J. Cryst. Growth*, 2005, **275**, 606–616.
- 35 L. W. Shacklette, T. R. Jow and L. Townsend, *J. Electrochem. Soc.*, 1988, **135**, 2669–2674.
- 36 K. Ufer, G. Roth, R. Kleeberg, H. Stanjek, R. Dohrmann and J. Bergmann, *Z. Kristallogr.*, 2004, **219**, 519–527.